Journal of Imaging Informatics in Medicine (2025) 39:1547–1557
https://doi.org/10.1007/s10278-025-01631-2

ORIGINAL PAPER

Development and Validation of an Explainable MRI-Based Habitat Radiomics Model for Predicting p53-Abnormal Endometrial Cancer: A Multicentre Feasibility Study

Wentao Jin[1] · Hao Zhang[2] · Yan Ning[3] · Xiaojun Chen[4] · Guofu Zhang[1] · Haiming Li[5,6] · He Zhang[1]

Received: 16 April 2025 / Revised: 12 July 2025 / Accepted: 21 July 2025 / Published online: 4 August 2025

Abstract

We developed an MRI-based habitat radiomics model (HRM) to predict p53-abnormal (p53abn) molecular subtypes of endometrial cancer (EC). Patients with pathologically confirmed EC were retrospectively enrolled from three hospitals and categorized into a training cohort ($n=270$), test cohort 1 ($n=70$), and test cohort 2 ($n=154$). The tumour was divided into habitat sub-regions using diffusion-weighted imaging (DWI) and contrast-enhanced (CE) images with the K-means algorithm. Radiomics features were extracted from T1-weighted imaging (T1WI), T2-weighted imaging (T2WI), DWI, and CE images. Three machine learning classifiers—logistic regression, support vector machines, and random forests—were applied to develop predictive models for p53abn EC. Model performance was validated using receiver operating characteristic (ROC) curves, and the model with the best predictive performance was selected as the HRM. A whole-region radiomics model (WRM) was also constructed, and a clinical model (CM) with five clinical features was developed. The SHApley Additive ExPlanations (SHAP) method was used to explain the outputs of the models. DeLong's test evaluated and compared the performance across the cohorts. A total of 1920 habitat radiomics features were considered. Eight features were selected for the HRM, ten for the WRM, and three clinical features for the CM. The HRM achieved the highest AUC: 0.855 (training), 0.769 (test1), and 0.766 (test2). The AUCs of the WRM were 0.707 (training), 0.703 (test1), and 0.738 (test2). The AUCs of the CM were 0.709 (training), 0.641 (test1), and 0.665 (test2). The MRI-based HRM successfully predicted p53abn EC. The results indicate that habitat combined with machine learning, radiomics, and SHAP can effectively predict p53abn EC, providing clinicians with intuitive insights and interpretability regarding the impact of risk factors in the model.

Keywords Endometrial cancer · Magnetic resonance imaging · Prognosis · Radiomics · Habitat

Introduction

Endometrial cancer (EC) is one of the most common gynaecological malignancies in developed countries. In East Asia, the incidence of EC has been rapidly increasing owing to changes in diet and lifestyle [1]. Owing to the frequent

Wentao Jin and Hao Zhang contributed equally to this work.

✉ Haiming Li
lihaiming0109@163.com

✉ He Zhang
zhanghe1790@fckyy.org.cn

[1] Department of Radiology, Obstetrics and Gynecology Hospital, Fudan University, Shanghai, People's Republic of China

[2] Department of Interventional Radiology, Fudan University Shanghai Cancer Center, Shanghai, People's Republic of China

[3] Department of Pathology, Obstetrics and Gynecology Hospital, Fudan University, Shanghai, People's Republic of China

[4] Department of Gynecology, Obstetrics and Gynecology Hospital, Fudan University, Shanghai, People's Republic of China

[5] Department of Radiology, Fudan University Shanghai Cancer Center, Shanghai, People's Republic of China

[6] Department of Oncology, Shanghai Medical College, Fudan University, Shanghai, People's Republic of China

presentation of early symptoms such as vaginal bleeding, most patients achieve histological diagnosis through minimally invasive diagnostic curettage and receive timely treatment. Consequently, the prognosis of EC is generally favourable, with satisfactory progression-free survival and overall survival rates. However, specific cases such as high-grade endometrioid carcinoma and serous carcinoma present with overlapping morphological and immunohistochemical (IHC) features that complicate risk stratification [2, 3]. In 2013, The Cancer Genome Atlas introduced the molecular subtypes of EC, revealing that certain subtypes, particularly non-endometrioid EC subtypes, are associated with poor prognoses. Compared with conventional histological classification, this molecular subtype system offers improved accuracy in evaluating prognosis and recurrence risk, thereby supporting the implementation of personalised treatment strategies. On the basis of the outcomes of TCGA and the ProMisE (Proactive Molecular Risk Classifier for EC), tumours are divided into four subgroups according to the presence of polymeraseepsilon (POLE) exonuclease domain mutations (EDMs) and p53 immunohistochemistry and mismatch repair (MMR) proteins, creating four different subgroups: DNA POLE, microsatellite instability-high/deficient mismatch repair (MSI-H/dMMR), copy-number-low/TP53-wild-type (CNL), and copy-number-high/TP53-mutant (CNH/p53abn) [4, 5]. Within this classification framework, the p53abn molecular subtype is included in the high-risk group [6–9].

Magnetic resonance imaging (MRI) is a widely used imaging method in clinical practice that serves as an essential tool for diagnosing, staging, post-treatment monitoring, and predicting therapeutic outcomes in EC [10]. However, its diagnostic capabilities are limited because overlapping imaging features are often observed among benign and malignant lesions and across different EC subtypes. Even radiologists with significant expertise in gynaecological oncology may face challenges in accurately identifying the pathological or molecular subtypes of EC [11], limiting its utility in guiding treatment decisions and providing precise prognostic predictions.

Recently, the number of radiomics studies focusing on the quantification of imaging data has increased. Radiomics extracts high-throughput features from medical images that are invisible to the naked eye, enabling the prediction of clinical outcomes, such as lesion classification, tumour staging, prognosis, and therapeutic response. Several studies have demonstrated the utility of MRI-based radiomics in aiding clinicians with EC grading and prognostic assessment [12–16]. In a review and meta-analysis on MRI radiomics in EC, the authors included 15 relevant studies from recent years, involving a total of 3608 patients. The study showed that radiomics demonstrated high sensitivity and specificity in predicting high-grade EC, deep myometrial invasion, lymphovascular space invasion, and lymph node metastasis [17]. However, traditional radiomics typically extracts global features from the entire region of interest (ROI), assuming the lesion is homogeneous, which substantially limits its ability to represent the tumour microenvironment. Recently, research on tumour habitats has drawn increasing attention. Compared with traditional radiomics, habitat analysis enables the segmentation of tumours into subregions based on intratumoural heterogeneity, allowing for a detailed analysis of features within these subregions [18–20]. To the best of our knowledge, no previous studies have utilised habitat analysis to predict the molecular subtypes of EC [2].

Therefore, this study aimed to construct a habitat radiomics model (HRM) for predicting p53abn EC and validate its performance in two independent test cohorts. We also employed the SHApley Additive ExPlanations (SHAP) value to explain the model, enabling clinicians to better understand the reasons behind the outcomes.

Materials and Methods

Patients

Patients with EC were retrospectively collected from FOGH from January 2019 to August 2022 as the training cohort, FSCC from January 2021 to January 2022 as test cohort 1, and BCYH from January 2022 to March 2023 as test cohort 2. Our Institutional Review Board approved this retrospective study, and the requirement for informed consent was waived for all participants. The inclusion criteria were preoperative pelvic MRI showing intrauterine masses and histologically confirmed EC. The exclusion criteria were as follows: (1) no detectable mass or minimal lesion (maximum diameter < 1 cm) on MRI, (2) MRI performed post-treatment, (3) MRI conducted at external institutions, (4) incomplete or poor-quality magnetic resonance images, and (5) lack of molecular subtype diagnostic results (Fig. 1). The clinical data of the enrolled patients were collected, including age, body mass index (BMI), CA125 level, tumour pathological diagnosis, Federation of Gynecology and Obstetrics staging (FIGO), and molecular subtype.

Image Acquisition and Interpretation

All basic scan protocols were used to image the entire pelvis, according to the European Society of Urogenital Radiology (7). MRI at FOGH was performed using a 1.5-T scanner (Magnetom Avanto, Siemens, Germany). MRI at FSCC was performed using a 3.0-T scanner (Magnetom Skyra, Siemens, Germany). MRI at BCYH was performed using 1.5-T scanners (Signa HDxt, General Electric Company, USA). Detailed parameters of the MRI sequences are

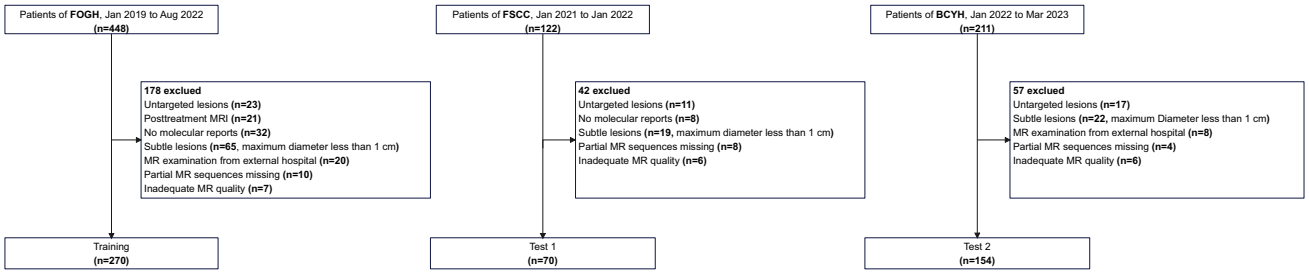

Fig. 1 Patient recruitment process

listed in Supplementary Table S1**.** The contrast agent was gadobutrol (Magnevist; Bayer Schering, Berlin, Germany) at an injection flow rate of 2 mL/s and a dose of 1 mL/kg body weight. The median time interval between MRI and surgery was 7 days (range, 1–33 days).

Image Preprocessing and Tumour Segmentation

N4 bias field correction was used for all images to reduce the nonuniformity of the magnetic field of the different MRI scanners. All images were resampled to isotropic voxels of $1 \times 1 \times 1$ mm^3 by B-spline interpolation. The open-source software ITK-SNAP (version 4.0, itksnap.org) was used to perform image registration between different sequences and for tumour segmentation. Axial T2-weighted (T2WI), T1-weighted (T1WI), and diffusion-weighted imaging (DWI) with higher b values (1000 or 800 s/mm^2) and contrast-enhanced (CE) images were matched by registration to guarantee spatial coherence within a common reference space. ROI segmentation was performed by senior physicians with 10 years of experience in MRI diagnostics to manually map the intratumoural region along the edge of the tumour, layer by layer, on T2WI.

Subregion Habitat Clustering

The K-means method was used to cluster the subregions based on the voxel values of the DWI and CE subtraction images. Each CE subtraction image was obtained by subtracting the pre-CE from the CE image on a voxel-by-voxel basis. The number of clusters from 2 to 10 was tested in this study. The optimal number of clusters was selected based on the Calinski–Harabasz (CH) value (Fig. 2).

Feature Extraction and Selection

The open-source Python package PyRadiomics (https://pypi.org/project/PyRadiomics/) was used to extract the radiomics features. Radiomics features of the tumour habitat were extracted from each subregion. Whole-region radiomics features were extracted from the entire ROI of the tumour. All the features extracted from the ROI were normalised and standardised using Z-score normalisation. Details of the

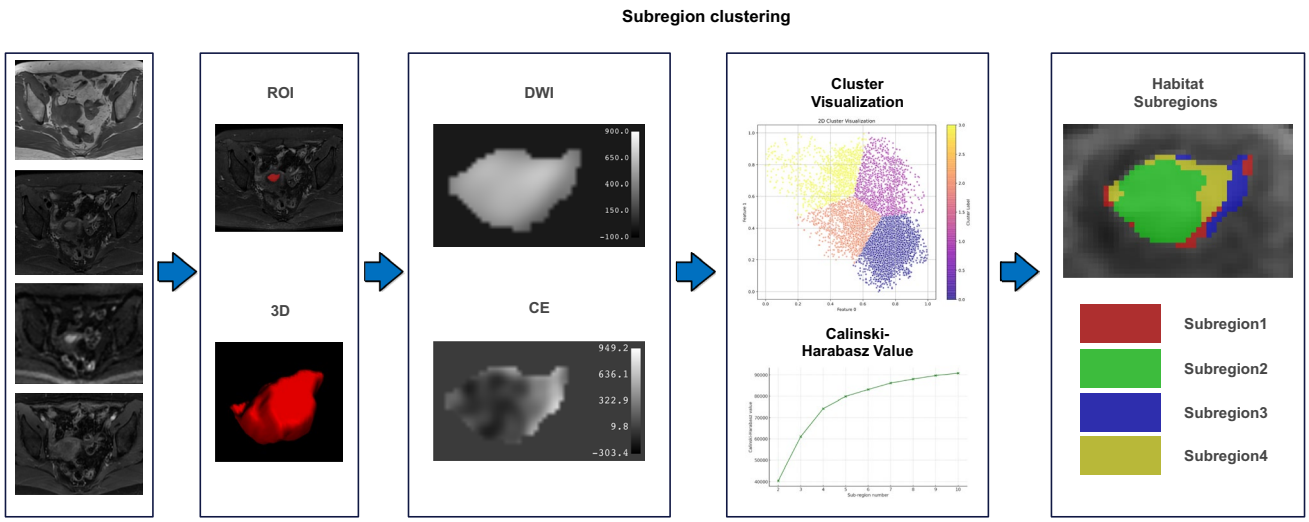

Fig. 2 Flowcharts of subregion clustering

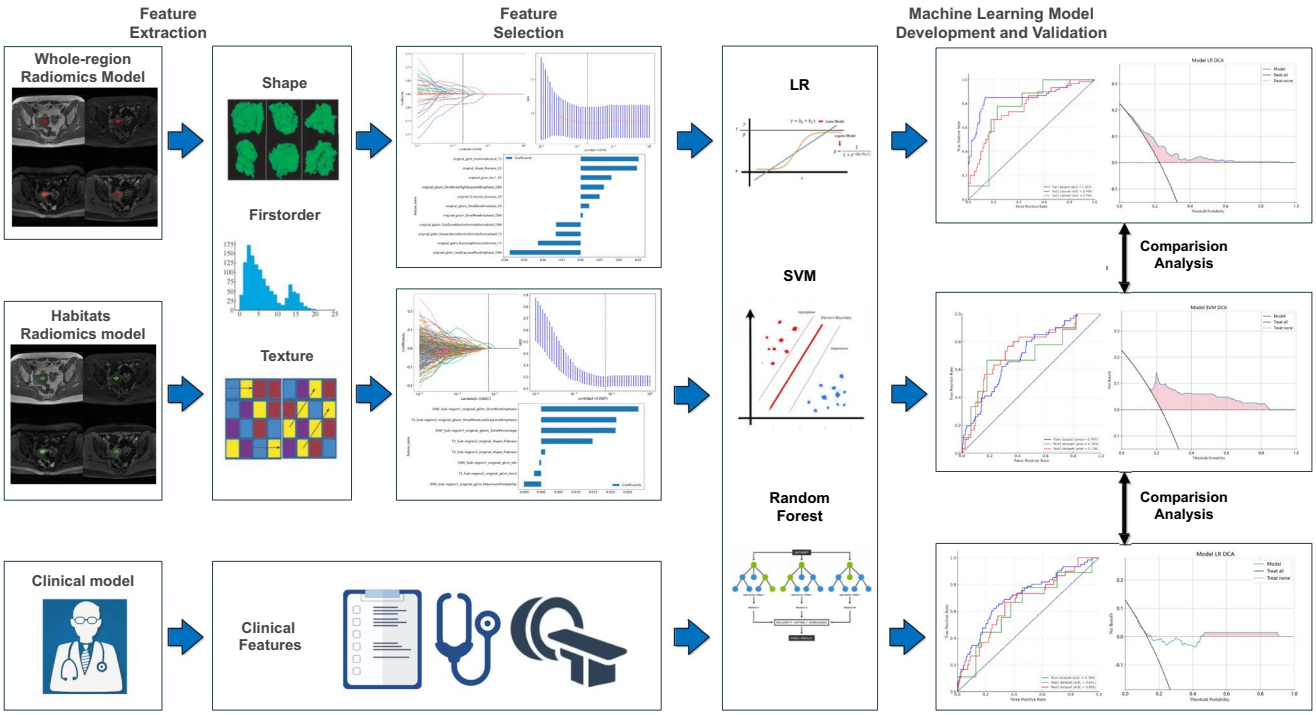

Fig. 3 Development, validation, and comparison of machine learning models

radiomics features are shown in Supplementary Note1. All patients in the training cohort were used to select the features and construct the prediction model. The features related to p53abn EC were identified using a three-step screening process. First, the features were subjected to rigorous statistical scrutiny and preliminary filtration using Student's *t*-test, with a retention criterion set for features exhibiting $p < 0.05$. Second, to circumvent the overrepresentation of highly collinear features, inter-feature correlations were evaluated using the Spearman correlation coefficient, and in instances of correlations exceeding 0.9, only one feature was retained. The final selection procedure involved least absolute shrinkage and selection operator (LASSO) regression. Tenfold cross-validation was used to tune the parameters to find the best λ value.

Construction, Validation, and Comparison of Multimachine Learning Models

The HRM was constructed using the final habitat radiomics features, and three machine-learning classifiers: logistic regression (LR), support vector machine (SVM), and random forest (RF). The model with the highest predictive performance was selected as the HRM. Model performance was investigated using receiver operating characteristic (ROC) curves.

Radiomics features extracted from the entire ROI were used to develop the whole-region radiomics model (WRM). We applied the same feature selection and model construction workflow to develop a WRM using the training cohort. The performances of the WRM and HRM were compared using DeLong's test.

Data on age, BMI, Ca125, maximum lesion diameters, and apparent diffusion coefficient (ADC) values of the patients were collected. The maximum diameter and ADC values were measured by two radiologists with 10 and 15 years of diagnostic experience. In cases of disagreement, the results were analysed through discussion. A clinical model (CM) was developed using the LR, SVM, and RF machine learning models with five clinical features. The performances of CM and HRM were compared using DeLong's test (Fig. 3).

Molecular Pathological Preparation, Reading, and Diagnosis

Paraffin sections were prepared for molecular pathology by cutting them into 5–15 white slides, each 5 microns thick. Tumour tissues were enriched to 60–80% by scraping with a scalpel blade. Total DNA was extracted using a magnetic bead nucleic acid extraction and purification kit (Burnstone Medical, Guangzhou, China), and DNA quality was assessed using the Nanodrop and Qubit platforms. Genetic analysis was performed using the ECG10-Panel (XIAMEN SPACEGEN CO., LTD., China), which targets key endometrial carcinoma genes, including *MSH2*, *PMS2*,

MLH1, *MSH6*, *EPCAM*, *POLE*, *Tp53*, *PTEN*, *PIK3CA*, *KRAS*, and 10 microsatellite loci. Sequencing data were processed and aligned to the hg19 reference genome using the Trimmomatic software (http://www.usadellab.org/cms/index.php?page=trimmomatic). A gynaecologic pathologist with extensive experience reviewed all samples for morphological and IHC results. Molecular biology and medical genetics experts collaboratively analysed and discussed the molecular test data to determine the molecular typing and establish a definitive diagnosis.

Interpretability Analysis of the HRM

SHAP was used to explain the HRM output. The SHAP summary plot shows the importance and distribution of SHAP values for each feature. A SHAP force plot was used to show the contributions of different features to a single case.

Statistical Analysis

The Mann–Whitney *U* test and chi-square test were used to compare differences in baseline data among patients. The details of the interclass correlation coefficients are presented in Supplementary Note2. The ROC curve was used to evaluate model performance. The prediction performances of the clinical and computerised models were also compared for both the training and test cohorts. All statistical analyses were performed using SPSS (version 21.0; IBM Corp., Armonk, NY, USA) and Python 3.9.7 (https://www.python.org/). The *p*-value was two-sided, and $p < 0.05$ was considered statistically significant.

Results

Baseline Data in the Training and Test Cohorts

A total of 494 patients were included in the study, of whom 92 (18.6%) had p53abn. A total of 270 patients were included in the training cohort, 70 in test cohort 1, and 154 in test cohort 2. The baseline data of the patients from different centres are provided in Table 1. In the training cohort from FOGH, the age difference between the p53abn EC and other groups was statistically significant, whereas no significant differences were observed for the other parameters (Table 1).

Subregion Clustering, Habitat Feature Extraction, and Selection

The line chart of the relationship between CH values and the number of clusters shows that the CH values increase gradually after four clusters; thus, four was selected as the optimal number of clusters (Fig. 2). The K-means method was applied to divide the tumour ROI into four subregions. The K-means algorithm considered DWI and CE image voxel values along with their relative spatial positions as features for clustering to avoid overly mixed partitions. Among the subregions, red (subregion 1) represented areas with comparatively low DWI and low CE voxel values, green (subregion 2) indicated areas with relatively high DWI and low CE voxel values, blue (subregion 3) corresponded to areas with relatively low DWI and high CE voxel values, and yellow (subregion 4) referred to areas with relatively high DWI and high CE voxel values. Subsequently, radiomic features were extracted from these four subregions in the T1WI, T2WI, DWI, and CE images, yielding 1920 habitat radiomic features. After a three-step selection process, eight habitat radiomic features were selected for model development (Supplementary Fig.S1). Classification was based on image sequences, with four features derived from DWI and four from T2WI. The classification was based on subregions, with four features derived from subregion 1, two from subregion 2, and two from subregion 3.

Development and Validation of the HRM

The eight habitat features were fed into three machine learning classifiers for model development. Among them, the RF model exhibited the highest area under the curve (AUC) in the training cohort (0.997, 95% CI 0.993–1.000); however, there was a noticeable decline in test cohort 1 (0.511, 95% CI 0.364–0.658) and test cohort 2 (0.542, 95% CI 0.320 – 0.764). We suspect that this could be attributed to data overfitting, which led us to exclude this model. Among the remaining two models, the SVM model consistently had higher AUC values (training: 0.855, 95% CI 0.788–0.922; test1: 0.769, 95% CI 0.631–0.907; test2: 95% CI 0.661–0.871) than the LR model (training: 0.733, 95% CI 0.663–0.803; test1: 0.632, 95% CI 0.414 – 0.850; test2: 0.596, 95% CI 0.398 – 0.793). Therefore, the SVM model was selected as the final HRM (Table 2).

Development of the WRM and CM and Comparison with the HRM

Whole-region radiomics features were extracted from the entire ROI of the tumour from the T1WI, T2WI, DWI, and CE images. In total, 480 features were collected

Table 1 Baseline data of patients

	Training ($n=270$)			Test1 ($n=70$)			Test2 ($n=154$)		
	p53abn	Others	*p*	p53abn	Others	*p*	p53abn	Others	*p*
N (%)	61 (22.59%)	209 (77.41%)		9 (12.86%)	61 (87.14%)		22 (14.29%)	132 (85.71%)	
Age, years	59 (51, 66)	53 (46, 58)	*0.001*	60 (54, 70)	54 (48, 59)	0.083	60 (57, 64)	58 (52, 66)	0.583
Body mass index, kg/m^2	24.17 (22.11, 26.56)	23.44 (21.78, 25.89)	0.421	25.48 (25.10, 25.85)	24.44 (22.60, 27.22)	0.598	27.01 (23.71, 29.83)	25.39 (23.05, 28.91)	0.158
CA125, U/mL	26.98 (13.00, 68.80)	23.50 (14.41, 39.96)	0.248	12.80 (11.10, 20.00)	18.40 (12.70, 27.20)	0.366	12.00 (9.68, 22.25)	15.45 (9.20, 29.73)	0.505
MAX diameter, cm	3.60 (2.40, 4.70)	3.30 (2.00, 4.70)	0.312	3.16 (2.03, 4.53)	2.72 (1.82, 4.23)	0.930	4.01(2.72, 4.77)	3.90 (3.38, 4.43)	0.473
ADC, 10^{-6}mm^2/s	861 (719,990)	870 (744, 1029)	0.078	867(804, 1018)	874 (744, 1048)	0.937	859(814, 974)	864 (779, 1107)	0.098

p53abn p53abnormal, *ADC* apparent diffusion coefficient

and incorporated into the feature selection process. The 11 best discriminative features were included in the construction of the WRM (Supplementary Fig.S2). We selected the LR model as the final WRM, with an AUC of 0.707 (0.637–0.778, 95% CI) in the training cohort, 0.703 (0.493–0.913, 95% CI) in test cohort 1, and 0.738

Table 2 Performance of multiple machine learning models

Model	Cohort	AUC	95% CI	Accuracy	Sensitivity	Specificity
Habitat Radiomics Model						
LR	**Training**	0.733	0.663–0.803	0.789	0.443	0.890
	Test1	0.632	0.414–0.850	0.643	0.667	0.650
	Test2	0.596	0.398–0.793	0.671	0.667	0.683
SVM	**Training**	0.855	0.788–0.922	0.863	0.852	0.866
	Test1	0.769	0.631–0.907	0.771	0.778	0.770
	Test2	0.766	0.661–0.871	0.763	0.667	0.795
RF	**Training**	0.997	0.993–1.000	0.989	0.889	0.305
	Test1	0.511	0.364–0.658	0.371	0.889	0.305
	Test2	0.542	0.320–0.764	0.471	0.778	0.433
Whole-region Radiomics Model						
LR	**Training**	0.707	0.637–0.778	0.596	0.803	0.536
	Test1	0.703	0.493–0.913	0.800	0.667	0.820
	Test2	0.738	0.629–0.847	0.691	0.767	0.672
SVM	**Training**	0.697	0.626–0.768	0.622	0.787	0.577
	Test1	0.652	0.486–0.819	0.414	1.000	0.328
	Test2	0.636	0.442–0.829	0.371	1.000	0.283
RF	**Training**	0.997	0.991–1.000	0.989	0.984	0.990
	Test1	0.609	0.410–0.808	0.314	1.000	0.217
	Test2	0.648	0.422–0.875	0.786	0.832	0.312
Clinical Model						
LR	**Training**	0.709	0.633–0.785	0.715	0.623	0.745
	Test1	0.641	0.430–0.853	0.571	0.778	0.541
	Test2	0.665	0.550–0.780	0.658	0.667	0.664
SVM	**Training**	0.725	0.649–0.800	0.759	0.574	0.813
	Test1	0.399	0.168–0.629	0.886	0.111	1.000
	Test2	0.518	0.333–0.703	0.486	0.667	0.467
RF	**Training**	0.999	0.997–1.000	0.967	1.000	0.957
	Test1	0.477	0.305–0.650	0.471	0.667	0.474
	Test2	0.588	0.414–0.763	0.386	1.000	0.295

LR logistic regression, *SVM* support vector machine, *RF* random forest

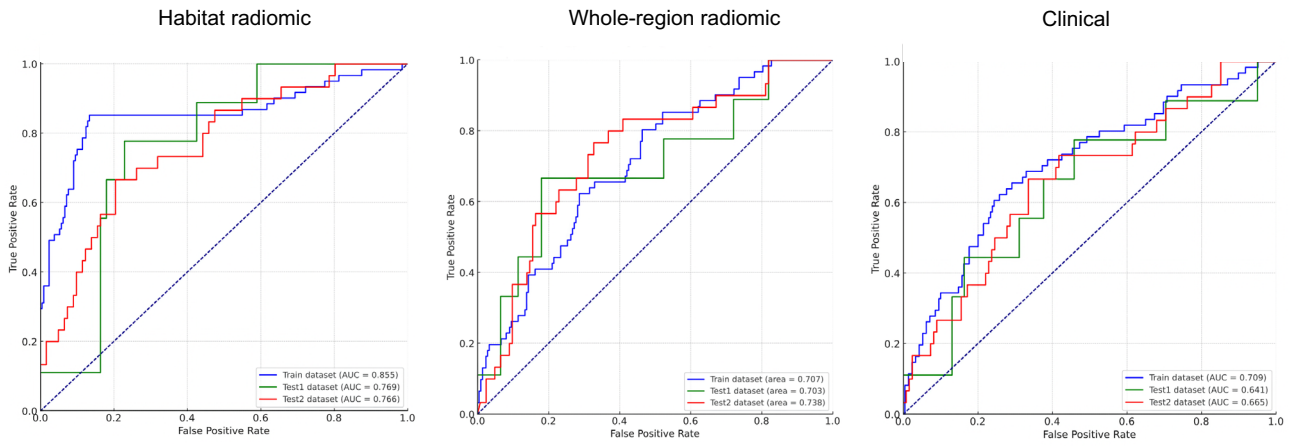

Fig. 4 ROCs of machine learning models

(0.629–0.847, 95% CI) in test cohort 2. DeLong's test indicated that the differences in the AUC between the WRM and HRM in training and test 2 were statistically significant (training: $p = 0.001$; test2: $p = 0.019$,), whereas no significant difference was observed in test 1 ($p = 0.680$).

Age, BMI, Ca125, maximum lesion diameters and ADC were included in the construction of the CM. The LR model exhibited the best predictive performance. The AUC was 0.709 (95% CI 0.633–0.785) in the training cohort, 0.641 (95%CI 0.430–0.853) in test cohort 1, and 0.665 (95% CI 0.550–0.780) in test cohort 2. DeLong's test indicated that the differences in the AUC between the WRM and HRM in the three cohorts were statistically significant (training: $p = 0.007$; test1: $p = 0.038$; test2: $p = 0.039$) (Fig. 4).

Interpretability Analysis of the HRM

The SHAP force plot was used for interpretability analysis of the individual samples (Fig. 5). The SHAP summary plot was used for the overall interpretability analysis of the model (Fig. 6) to show the impact of each feature on the model predictions.

Discussion

Compared to traditional histological subtyping, molecular subtyping provides a more accurate indication of prognosis for EC patients. p53abn is commonly observed in serous carcinoma, clear cell carcinoma, carcinosarcoma, and mixed carcinoma and is associated with higher malignancy. Molecular diagnosis of EC usually requires complex procedures, additional time, and high costs and is not routinely performed, even in certain academic medical centres. Owing to its excellent soft-tissue resolution, MRI is widely used for EC diagnosis and staging. However, radiologists cannot accurately determine the histological and molecular subtypes of EC using MRI. In recent years, MRI-based radiomics research has increased, enabling the extraction of imaging features imperceptible to the human eye and allowing for a more accurate evaluation and analysis of disease characteristics [21, 22]. Studies have shown that radiomics methods achieve high accuracy in predicting lymphovascular space invasion. Previous studies have used tumour habitats to reflect the degree of glioma infiltration [20, 23, 24]. Compared with the traditional whole ROI, the habitat subregion offers the advantage of dividing the tumour into subregions with similar characteristics based on the specific properties of the tumour. Radiomic features can then be separately extracted from each subregion, enabling a more precise evaluation of tumour heterogeneity [25, 26]. However, no studies have reported the use of habitat to predict molecular subtypes of EC. We applied the habitat to intratumoural partitioning in EC and extracted multiparametric MRI-based radiomic features from each subregion. Predictive models were built using multiple machine learning models, achieving high accuracy in noninvasively predicting p53abn EC. Compared with previous studies, the habitat method more accurately captured regional heterogeneity and the tumour microenvironment. Moreover, our model predicted the p53abn subtype associated with poor prognosis in EC, demonstrating considerable clinical value in the diagnosis and management.

In this study, EC tumours were divided into four habitat subregions using DWI and CE images. DWI reflects the cellular density of the tumour, whereas CE indicates tumour vascularity. Multimodal habitat partitioning using these two imaging modalities allows the division of the lesion into subregions with varying levels of cellular density and blood

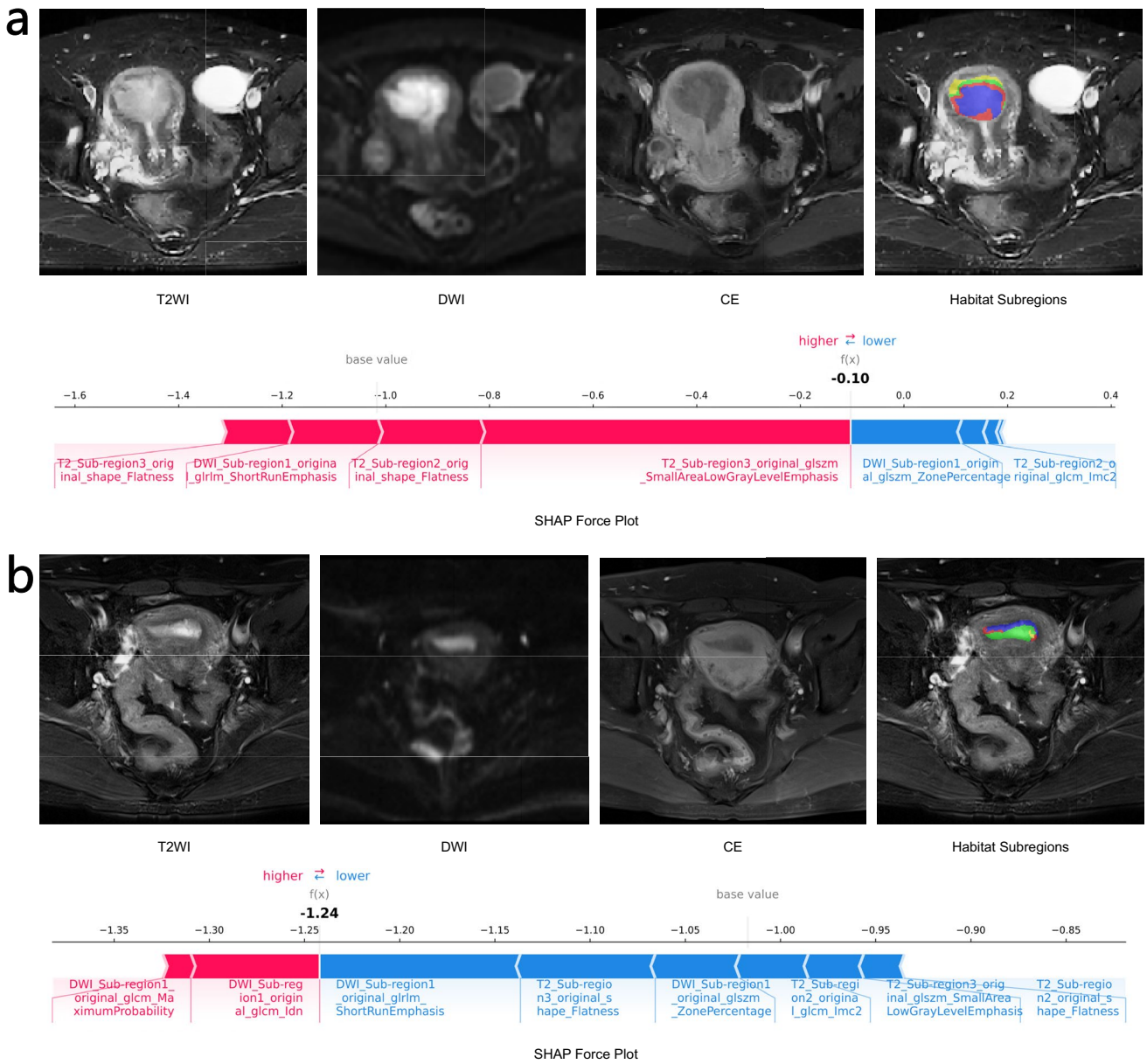

Fig. 5 Case a, with HRM model predicting a 69.8% probability of p53abn EC. histotype: uterine Carcinosarcoma; deep myometrial invasion; lymphovascular space invasion(+)/cervical invasion(+)/lymph node metastasis(+); Molecular type: p53abn. The SHAP force plot is predominantly characterized by rightward red arrows, indicating that these features positively contribute to the outcome and increase the predicted value, suggesting a higher likelihood of the p53abn EC. The Glszm_SmallAreaLowGrayLevelEmphasis feature in subregion 3 (blue) of the T2WI image has the highest weight. Case b, with HRM model predicting a 19.5% probability of p53abn EC. histotype: endometrioid carcinoma of the endometrium; superficial myometrial invasion; lymphovascular space invasion(-)/cervical invasion(-)/lymph node metastasis(-); Molecular type: MSI-H. The SHAP force plot is predominantly characterized by leftward blue arrows, indicating that these features negatively contribute to the outcome, decreasing the predicted value and suggesting a lower probability of p53abn EC. The Glrlm_ShortRunEmphasis feature in subregion 1 (red) of the DWI image has the highest weight

supply [27, 28]. In a study by Syed et al., habitat was used to predict treatment outcomes in patients with HER2-positive breast cancer, and DWI and CE images were used for habitat segmentation [29]. In our study, k-means clustering was applied to the subregion segmentation. This method provides a relatively good spatial continuity, minimises the occurrence of mixed subregions, and yields stable and reproducible results [13]. However, as it is an unsupervised algorithm, the interpretability of the results requires further investigation. After segmenting the habitat subregions, radiomic features were extracted from each subregion, and HRM showed better predictive performance than the WRM and CM. This improvement may be due to the WRM approach, which encompasses necrotic or benign regions that cannot

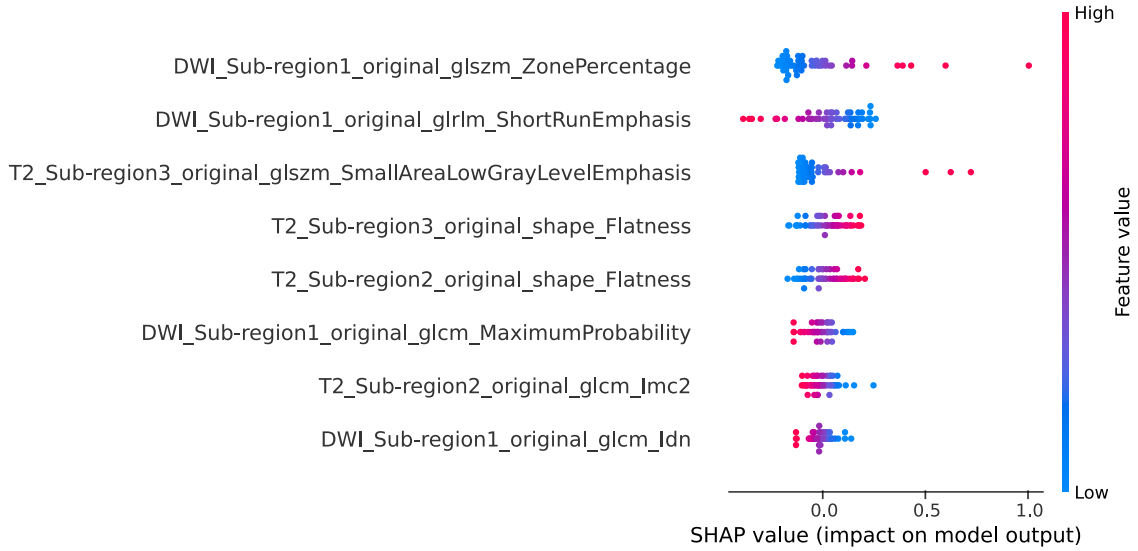

Fig. 6 SHAP summary plot of HRM. The plot shows that the feature ZonePercentage from sub-region1 of DWI is the most important for the HRM, and as its feature value decreases, the predicted probability of p53abn increases

accurately represent tumour malignancy. If these regions are included in feature extraction alongside malignant regions, the diagnostic accuracy is inevitably affected. The habitat subregion reduces this impact and highlights the inherent heterogeneity within the tumour [30, 31]. In our study, the ZonePercentage (ZP) from subregion 1 of DWI showed the highest value among the eight habitat radiomics features based on SHAP. From a physical standpoint, the ZP reflects the balance between the number of contiguous, uniform-intensity regions within the ROI and the total voxel count. A higher ZP indicates that the ROI is split into numerous smaller homogeneous zones, resulting in a more fragmented texture, whereas a lower ZP indicates more coherent and uniform regions. In medical images, a higher ZP is suggestive of a tumour with a more uneven texture and a mixed distribution of cell density, implying greater heterogeneity and potentially indicating a higher level of aggressiveness or rapid growth. Among the eight habitat features, four were derived from subregion 1 with low DWI and CE voxel values, suggesting that the MRI features of regions with high cellular density and low vascularity have a greater predictive significance for p53abn EC. This study also revealed that the AUC of the HRM was higher than that of the WRM and CM. However, the AUC difference between the HRM and WRM was not statistically significant in test cohort 2, possibly because of the small external validation sample size and the low positive rate of p53abn, which may have introduced a statistical bias.

This study had several limitations. First, as a multicentre study, the sample size was relatively limited, particularly in the test cohort 1. Second, this study focused solely on distinguishing p53abn from other molecular subtypes. Third, the study relied on manual segmentation of tumour ROIs by physicians, which may introduce variability owing to differences in physician experience, potentially affecting the model's performance. Future research should investigate deep learning-based automatic ROI segmentation to improve reproducibility and model generalisability.

In conclusion, MRI-based HRM demonstrated relatively accurate prediction of p53abn EC, outperforming the conventional WRM and CM in terms of predictive efficacy. The results indicate that the habitat method combined with machine learning, radiomics, and SHAP can effectively predict p53abn EC, providing clinicians with intuitive insights and interpretability regarding the impact of risk factors in the model.

Supplementary Information The online version contains supplementary material available at https://doi.org/10.1007/s10278-025-01631-2.

Acknowledgements Throughout the writing of this dissertation, I have received a great deal of support and assistance. I would first like to thank He Zhang and Haiming Li, whose expertise was invaluable in formulating the research questions and methodology. Your insightful feedback pushed me to sharpen my thinking and brought my work to a higher level. I would particularly like to acknowledge my team members, Hao Zhang, Yan Ning, and Xiaojun Chen, for their wonderful collaboration and patient support. I would also like to thank my chief, Guofu Zhang, for his valuable guidance throughout my studies. You provided me with the tools that I needed to choose the right direction and successfully complete my dissertation. In addition, I would like to thank my parents for their wise counsel and sympathetic ear. You are always there for me. Finally, I could not have completed this dissertation without the support of my friends and wife, who provided stimulating discussions as well as happy distractions to rest my mind outside of my research.

Author Contribution All authors contributed to the study conception and design. Material preparation, data collection, and analysis were performed by Wentao Jin, Hao Zhang, Yan Ning, Xiaojun Chen, Guofu Zhang, Haiming Li, and He Zhang. The first draft of the manuscript was written by Wentao Jin, and all authors commented on previous versions of the manuscript. All authors read and approved the final manuscript.

Funding This work was funded by the Shanghai Natural Science Foundation (grant No. 25ZR1401036).

Data Availability All data is available in our database and it can be supplied in case of some necessary.

Declarations

Competing Interests The authors declare no competing interests.

Ethics Approval This is an observational study. The Obstetrics and Gynecology Hospital of Fudan University Research Ethics Committee has confirmed that no ethical approval is required.

Consent to Participate Informed consent was obtained from all individual participants included in the study.

Consent for Publication The authors affirm that human research participants provided informed consent for publication of the images in Figs. 2, 3, and 5.

References

1. Crosbie EJ, Kitson SJ, McAlpine JN, Mukhopadhyay A, Powell ME, Singh N: Endometrial cancer. Lancet 399: 1412-1428, 2022
2. Jamieson A, Thompson EF, Huvila J, Gilks CB, McAlpine JN: p53abn endometrial cancer: understanding the most aggressive endometrial cancers in the era of molecular classification. Int J Gynecol Cancer 31: 907-913, 2021
3. Soslow RA, Tornos C, Park KJ, Malpica A, Matias-Guiu X, Oliva E, Parkash V, Carlson J, McCluggage WG, Gilks CB: Endometrial carcinoma diagnosis: use of FIGO grading and genomic subcategories in clinical practice: recommendations of the international society of gynecological pathologists. Int J Gynecol Pathol 38: S64-S74, 2019
4. Besharat AR, Giannini A, Caserta D: Pathogenesis and treatments of endometrial carcinoma. Clin Exp Obstet Gynecol 50: 229, 2023
5. D'Oria O, Giannini A, Besharat AR, Caserta D: Management of endometrial cancer: molecular identikit and tailored therapeutic approach. Clin Exp Obstet Gynecol 50: 210, 2023
6. Jamieson A, Thompson EF, Huvila J, Leung S, Lum A, Morin C, Ennour-Idrissi K, Sebastianelli A, Renaud MC, Gregoire J, Huntsman DG, Gilks CB, Plante M, Grondin K, McAlpine JN: Endometrial carcinoma molecular subtype correlates with the presence of lymph node metastases. Gynecol Oncol 165: 376-384, 2022
7. Raffone A, Travaglino A, Raimondo D, Neola D, Renzulli F, Santoro A, Insabato L, Casadio P, Zannoni GF, Zullo F, Mollo A, Seracchioli R: Prognostic value of myometrial invasion and TCGA groups of endometrial carcinoma. Gynecol Oncol 162: 401-406, 2021
8. Travaglino A, Raffone A, Mascolo M, Guida M, Insabato L, Zannoni GF, Zullo F: Clear cell endometrial carcinoma and the TCGA classification. Histopathology 76: 336-338, 2020
9. Murali R, Soslow RA, Weigelt B: Classification of endometrial carcinoma: more than two types. Lancet Oncol 15: e268-e278, 2014
10. Maheshwari E, Nougaret S, Stein EB, Rauch GM, Hwang KP, Stafford RJ, Klopp AH, Soliman PT, Maturen KE, Rockall AG, Lee SI, Sadowski EA, Venkatesan AM: Update on MRI in evaluation and treatment of endometrial cancer. Radiographics 42: 2112-2130, 2022
11. Nougaret S, Horta M, Sala E, Lakhman Y, Thomassin-Naggara I, Kido A, Masselli G, Bharwani N, Sadowski E, Ertmer A, Otero-Garcia M, Kubik-Huch RA, Cunha TM, Rockall A, Forstner R: Endometrial cancer MRI staging: updated guidelines of the European Society of Urogenital Radiology. Eur Radiol 29: 792-805, 2019
12. Lefebvre TL, Ciga O, Bhatnagar SR, Ueno Y, Saif S, Winter-Reinhold E, Dohan A, Soyer P, Forghani R, Siddiqi K, Seuntjens J, Reinhold C, Savadjiev P: Predicting histopathology markers of endometrial carcinoma with a quantitative image analysis approach based on spherical harmonics in multiparametric MRI. Diagn Interv Imaging 104: 142-152, 2023
13. Xie C, Yang P, Zhang X, Xu L, Wang X, Li X, Zhang L, Xie R, Yang L, Jing Z, Zhang H, Ding L, Kuang Y, Niu T, Wu S: Sub-region based radiomics analysis for survival prediction in oesophageal tumours treated by definitive concurrent chemoradiotherapy. EBioMedicine 44: 289-297, 2019
14. Ma X, Shen M, He Y, Ma F, Liu J, Zhang G, Qiang J: The role of volumetric ADC histogram analysis in preoperatively evaluating the tumour subtype and grade of endometrial cancer. Eur J Radiol 140: 109745, 2021
15. Chen X, Wang Y, Shen M, Yang B, Zhou Q, Yi Y, Liu W, Zhang G, Yang G, Zhang H: Deep learning for the determination of myometrial invasion depth and automatic lesion identification in endometrial cancer MR imaging: a preliminary study in a single institution. Eur Radiol 30: 4985-4994, 2020
16. Yan BC, Li Y, Ma FH, Feng F, Sun MH, Lin GW, Zhang GF, Qiang JW: Preoperative assessment for high-risk endometrial cancer by developing an MRI- and clinical-based radiomics nomogram: a multicenter study. J Magn Reson Imaging 52: 1872-1882, 2020
17. Di Donato V, Kontopantelis E, Cuccu I, Sgamba L, Golia D'Augè T, Pernazza A, Della Rocca C, Manganaro L, Catalano C, Perniola G, Palaia I, Tomao F, Giannini A, Muzii L, Bogani G: Magnetic resonance imaging-radiomics in endometrial cancer: a systematic review and meta-analysis. Int J Gynecol Cancer 33: 1070-1076, 2023
18. Kim M, Park JE, Kim HS, Kim N, Park SY, Kim YH, Kim JH: Spatiotemporal habitats from multiparametric physiologic MRI distinguish tumor progression from treatment-related change in post-treatment glioblastoma. Eur Radiol 31: 6374-6383, 2021
19. Lee DH, Park JE, Kim N, Park SY, Kim YH, Cho YH, Kim HS: Tumor habitat analysis by magnetic resonance imaging distinguishes tumor progression from radiation necrosis in brain metastases after stereotactic radiosurgery. Eur Radiol 32: 497-507, 2022
20. Verma R, Correa R, Hill VB, Statsevych V, Bera K, Beig N, Mahammedi A, Madabhushi A, Ahluwalia M, Tiwari P: Tumor habitat-derived radiomic features at pretreatment MRI that are prognostic for progression-free survival in glioblastoma are associated with key morphologic attributes at histopathologic examination: a feasibility study. Radiol Artif Intell 2: e190168, 2020
21. Huvila J, Pors J, Thompson EF, Gilks CB: Endometrial carcinoma: molecular subtypes, precursors and the role of pathology in early diagnosis. J Pathol 253: 355-365, 2021
22. Kather JN, Heij LR, Grabsch HI, Loeffler C, Echle A, Muti HS, Krause J, Niehues JM, Sommer KAJ, Bankhead P, Kooreman LFS, Schulte JJ, Cipriani NA, Buelow RD, Boor P, Ortiz-Brüchle NN, Hanby AM, Speirs V, Kochanny S, Patnaik A,

Srisuwananukorn A, Brenner H, Hoffmeister M, van den Brandt PA, Jäger D, Trautwein C, Pearson AT, Luedde T: Pan-cancer image-based detection of clinically actionable genetic alterations. Nat Cancer 1: 789-799, 2020

23. Jeong SY, Park JE, Kim N, Kim HS: Hypovascular cellular tumor in primary central nervous system lymphoma is associated with treatment resistance: tumor habitat analysis using physiologic MRI. AJNR Am J Neuroradiol 43: 40-47, 2022
24. Verma R, Hill VB, Statsevych V, Bera K, Correa R, Leo P, Ahluwalia M, Madabhushi A, Tiwari P: Stable and discriminatory radiomic features from the tumor and its habitat associated with progression-free survival in glioblastoma: a multi-institutional study. AJNR Am J Neuroradiol 43: 1115-1123, 2022
25. Cho HH, Kim H, Nam SY, Lee JE, Han BK, Ko EY, Choi JS, Park H, Ko ES: Measurement of perfusion heterogeneity within tumor habitats on magnetic resonance imaging and its association with prognosis in breast cancer patients. Cancers 14: 1858, 2022
26. Wang X, Xu C, Grzegorzek M, Sun H: Habitat radiomics analysis of pet/ct imaging in high-grade serous ovarian cancer: Application to Ki-67 status and progression-free survival. Front Physiol 13: 948767, 2022
27. Gaustad JV, Hauge A, Wegner CS, Simonsen TG, Lund KV, Hansem LMK, Rofstad EK: DCE-MRI of tumor hypoxia and hypoxia-associated aggressiveness. Cancers 12: 1979, 2020
28. Shih IL, Yen RF, Chen CA, Cheng WF, Chen BB, Chang YH, Cheng MF, Shih TT: PET/MRI in cervical cancer: associations between imaging biomarkers and tumor stage, disease progression, and overall survival. J Magn Reson Imaging 53: 305-318, 2021
29. Syed AK, Whisenant JG, Barnes SL, Sorace AG, Yankeelov TE: Multiparametric analysis of longitudinal quantitative MRI data to Identify distinct tumor habitats in preclinical models of breast cancer. Cancers 12: 1682, 2020
30. Dextraze K, Saha A, Kim D, Narang S, Lehrer M, Rao A, Narang S, Rao D, Ahmed S, Madhugiri V, Fuller CD, Kim MM, Krishnan S, Rao G, Rao A: Spatial habitats from multiparametric MR imaging are associated with signaling pathway activities and survival in glioblastoma. Oncotarget 8: 112992-113001, 2017
31. Tabassum M, Suman AA, Suero Molina E, Pan E, Di Ieva A, Liu S: Radiomics and machine learning in brain tumors and their habitat: a systematic review. Cancers 15: 3845, 2023